

Published in final edited form as:

Biomater Sci. 2018 June 25; 6(7): 1962–1975. doi:10.1039/c8bm00319j.

Bioinspired multilayer membranes as potential adhesive patch for skin wound healing

Maria P. Sousa^a, Ana I. Neto^{b,c}, Tiago R. Correia^d, Sónia P. Miguel^d, Michiya Matsusaki^e, Ilídio J. Correia^d, and João F. Mano^{a,b,c,*}

^aCICECO—Aveiro Institute of Materials, Department of Chemistry, University of Aveiro, 3810-193 Aveiro, Portugal

^b3B's Research Group, Biomaterials, Biodegradables and Biomimetics, University of Minho, Headquarters of the European Institute of Excellence on Tissue Engineering and Regenerative Medicine, AvePark-Parque de Ciência e Tecnologia, 4805-017 Barco, Taipas, Guimarães, Portugal

^cICVS/3B's, Associate PT Government Laboratory, Braga/Guimarães, Portugal

^dCICS-UBI—Health Sciences Research Centre University of Beira Interior- Covilhã-Portugal

^eDepartment of Applied Chemistry, Graduate School of Engineering, Osaka University, 2-1 Yamadaoka, Suita, Osaka 565-0871, Japan

Abstract

Bioinspired and adhesive multilayer membranes are produced using the layer-by-layer (LbL) assembly of chitosan (CHT), alginate (ALG) and hyaluronic acid modified with dopamine (HA-DN). Freestanding multilayer membranes without DN are also produced as a control. The success of the synthesis of HA-DN was confirmed using UV-visible spectroscopy. Scanning electron microscopy images indicate that the surface of the DN-containing membranes is quite more porous than the control ones; they also present a higher average thickness value for the same number of CHT/ALG/CHT/HA(-DN) tetralayers (n=100). Also, water uptake, mechanical strength and adhesion are enhanced with the introduction of DN moieties along the nano-layers. Besides, human dermal fibroblasts viability, enhanced adhesion and proliferation were confirmed by immunofluorescence assays and by measuring both metabolic activity and DNA content. Moreover, *in vivo* assays with such kind of DN-containing multilayer membranes were performed; the application of these membranes in the treatment of dermal wounds induced in Wistar rats results on the highest decreasing of inflammation of skin rat, compared with the control conditions. Overall, this investigation suggests that these mussel-inspired freestanding multilayer membranes may enhance either their mechanical performance as well as cellular adhesion and proliferation, leading to an improved wound healing process, being a promising material to restore the structural and functional properties of wounded skin.

* Author for correspondence. jmano@ua.pt.

Conflicts of interest

There are no conflicts to declare.

Introduction

Skin is the largest and most exposed organ in humans, serving as a protective barrier to the remaining organs against pathogens, virus, microorganisms as well as certain environmental conditions (chemical, mechanical or thermal constraints) 1–3. Accordingly, skin can be always an open door to potentially harmful impairments or agents, resulting in non-healing wounds. Skin is a vascular tissue, with ability to regenerate; however, a skin's injury with a diameter higher than 4 centimeter will be incapable to heal without an external support 4. For many years, donor skin grafting has been used as gold standard to treat such kind of skin defects, but the availability of donors is limited and restricted 2. Therefore, skin tissue engineering field has been growing during the last decades to create substitutes that mimic skin, towards clinical solutions that promote wound healing 5, 6. Ideally, tissue engineering combines the development of a support material with specific cells and bioactive agents to generate functional *in vitro* tissues that could be then transposed for the clinical practice 7.

For wound dressing, there are important specificities to meet; besides being non-toxic and non-allergic, these materials must be permeable to gas and provide a moist environment, protecting wounds from microbial action and absorbing resulting exudates 8, 9. Scientists have been pursuing materials that mimics the functional and structural features of the native extracellular matrix (ECM) of skin, serving as a barrier like epidermis and providing mechanical stability and elasticity like dermis 9. There are already some commercially available products; for instance, a hyaluronic acid (HA) ester bilayer scaffold (Hyalograft3D[®]) can be combined with an epidermal replacement autograft (Laserskin[®]) to permit wound closure 10. However, commercially available products must overpass the high production costs, the need of an additional fixation strategy, the risk of infection as well as the surgical intervention times 11. Therefore, to overcome such limitations other strategies have been investigated to design scaffolds for skin wound dressing, such as fibrous membranes 12, porous structures 13, hydrogels 14, 15, composites 16 or microparticles 17. However, these strategies usually encompass also some drawbacks as immune rejection for acellular scaffolds, poor cell adhesion for composite materials, limited mechanical strength in the case of hydrogels or the lack of interconnectivity in the case of porous scaffolds 18.

Layer-by-layer (LbL) technique is a quite simple technology to construct stable multilayer films by sequential adsorption of complementary multivalent molecules above a surface. The assembly of the different layers can be a result of covalent and/or noncovalent interactions, but, among the others, electrostatic driving forces have gained a key role 19. LbL stands out from other methodologies by its versatility, cost-effectiveness, robustness, ability to integrate a wide range of organic and inorganic materials and finely control the multiscale architecture 19–21. For instance, Guthrie K. M. *et al.* 22 incorporated silver nanoparticles within polyelectrolyte multilayers, constructed above elastomeric poly(dimethylsiloxane) (PDMS) sheets, to apply to the wounds beds of normal and diabetic mice and proved the feasibility of LbL-based substrates to improve wound healing. LBL films can be assembled in any type of substrate (regardless of size, shape or even surface geometry) and in certain occasions the template can be removed to generate a multilayer film that may retain the shape of the underlying substrate without the need of their physical support when implanted 23. In this

sense, more than coatings LbL methodology can render free-template materials like capsules 24, compartmentalized 25 and tubular 26 structures or even freestanding membranes 27, 28. Mamedov A. A. *et al.* 29 suggested the LbL assembly of alternating layers of magnetite nanoparticles and poly(diallyldimethylammonium bromide) above a cellulose acetate substrate, that was further dissolved in acetone, to obtain freestanding multilayer films. Herein, LbL technique is used to fabricate a free-template multilayer patch to treat skin wounds, without the need of using any organic solvent or compromising the integrity, the composition and the mechanical properties of the membrane.

To better control the physicochemical cell-material interactions and improve the biocompatibility, different strategies have been suggested; for instance, one can modify the chemistry of the surface with specific motifs³⁰, increase the hydrophilicity of the surface 31 or even create a topography suitable to generate a cell response 32. In the last decades, biomimetic materials have boosted tissue engineering and regenerative medicine field 33, 34, with different suitable properties of materials being inspired in natural systems. In particular, friendly bioadhesive systems have been proposed based on natural phenomena chasing their effectiveness 35. For instance, gecko's ability to adhere temporary to surfaces has been caught the attention of many scientists, which have been trying to reproduce the nanoscale topography of their foot pads; Lee H. *et al.* 36 developed a hybrid biologically-inspired adhesive material composed of an array of nanofabricated polymer pillars to mimic the nanoarchitecture organization of the gecko's foot pads. To improve the wet adhesion and durability, the authors coated the gecko-inspired pillars with a thin layer of a synthetic polymer, that mimics the wet adhesive proteins found in mussel holdfasts. In fact, mussels are other class of materials that has been nowadays very attracting to inspire bioadhesive systems. Mussels' ability to bond to any type of organic and inorganic substrate relies on their byssal threads' secretion of particular proteins, which amino acid content analysis showed the repetition of the 3,4-dihydroxyphenyl-alanine (DOPA) residue³⁷. Molecules containing catechols groups, such as DOPA or dopamine have been used to functionalize polymers, such as chitosan (CHT) and HA; for instance, Ryu J. H. *et al.* 38 suggested a new thermo-sensitive and injectable DOPA modified CHT/pluronic hydrogels and showed that these hydrogels exhibit excellent tissue-adhesion properties with superior *in vivo* gel stability; Hong S. *et al.* 39 produced HA-dopamine hydrogels found to be highly compatible with neural stem cells, presenting better viability and cell adhesion compared to the existing HA hydrogels. We hypothesized that the development of adhesive materials could enhance the performance of our freestanding multilayer system, by adhering to the tissue with improved cell adhesive properties.

In this investigation, CHT, a polycation derived from marine crustaceans, as well as alginate (ALG), a polyanion derived from algae, and hyaluronic acid (HA), a polyanion that is also part of the native ECM and plays an important role on mechanical and structural support, were electrostatically combined to produce multilayer polyelectrolyte films. Moreover, getting inspiration from marine mussels, HA was modified with dopamine by carbodiimide chemistry and combined with CHT and ALG to produce self-supportive freestanding multilayer membrane, that could be readily applied for skin wound healing. Neto A. I. *et al.* 40 already developed a high-throughput screening platform to characterize arrays of multilayer films containing dopamine-modified HA in terms of mechanical adhesion and

biological response. It was found that the introduction of the catechol groups in the multilayers clearly had a beneficial effect on adhesion and on cell adhesion and spreading. We hypothesize that such kind of multilayers could be transposed into multilayered membranes to be used as skin wound dressings. In this work both *in vitro* (morphology, mechanical properties, biofilm bacterial formation, adhesiveness, dermal cellular behavior) and *in vivo* (full thickness wounds in rats) characterization will be performed to assess the potential of such polysaccharide-based and biomimetic freestanding multilayer membranes.

Materials and Methods

Materials

CHT (Sigma, St. Louis, Missouri, United States of America(USA)) with a molecular weight in the range of 190–310 kDa, a N-deacetylation degree ranging from 75-85% and a viscosity of 0.2-0.8 Pa.s was purified following a standard procedure reported elsewhere 41. Sodium alginate (ALG) with a viscosity of 0.005-0.04 Pa.s and obtained from brown algae, hyaluronic acid (HA) with a molecular weight of 595 kDa as hyaluronic acid sodium salt from Streptococcus equi, dopamine hydrochloride (DN) and N-(3-Dimethylaminopropyl)-N'-ethylcarbodiimide hydrochloride (EDC) (purum, 98.0% (AT)) were purchased from Sigma and used as received.

Synthesis of HA-DN

HA-DN conjugates were synthesized using EDC as an activation agent of the carboxyl groups on HA chains, based on an already reported procedure 40 (see Figure S1). To avoid oxidation, the conjugated was stored at -20 °C and protected from the light until using.

Ultraviolet-visible (UV) Spectrophotometry—The degree of substitution of dopamine in the conjugate was determined using a UV-vis spectrophotometer (JascoV560 PC, Easton, Maryland, USA) and 1 cm quartz cells. Polymer solutions of 0.5 mg. mL⁻¹ in 0.15 M sodium chloride (NaCl, LabChem Inc, Zelienople, Pennsylvania, USA) were prepared for the UV-vis analyses.

¹H-Nuclear Magnetic Resonance (NMR)—¹H-NMR analyses were performed dissolving overnight the HA and the conjugated HA-DN in deuterated water (D₂O, Cambridge Isotope Laboratories, Inc.) at a concentration of 1 mg. mL⁻¹. The spectra were obtained using a spectrometer BRUKER BioSpin - 300 MHz, at 298 K and 300 MHz for ¹H.

Zeta (ζ)-potential measurements of polysaccharide solutions

Solutions of CHI (0.5 mg mL⁻¹), ALG (0.5 mg mL⁻¹), HA and HA-DN (0.25 mg mL⁻¹) containing NaCl (0.15 M) were prepared. The pH of the solutions was adjusted to 5.5. The ζ-potential of each solution was determined using a Nano range equipment from Malvern (United Kingdom), at 25 °C.

Quartz Crystal Microbalance with dissipation (QCM-D) monitoring

The formation of the multilayers of CHT/ALG/CHT/HA-DN was followed *in situ* by QCM-D (Q-Sense, Biolin Scientific, Göteborg, Sweden). The mass change results from the variation of the normalized resonant frequency ($f\nu$) of an oscillating quartz crystal when adsorption occurs on the surface and the dissipation factor (D) provides a measure of the energy loss in the system. If a rigid mass is adsorbed onto the surface of the piezoelectric crystal, there will be a decrease in the oscillation frequency. For viscoelastic materials, the adsorbed mass does not fully couple to the oscillation of the crystal, damping the oscillation. QCM-D allows simultaneously measuring the changes in the resonant frequency and in the viscoelastic properties (dissipation) when a film is adsorbed at the crystal surface. The measurements can be conducted at the fundamental frequency and at several overtones number ($\nu = 1,3,5,7,9,11$). CHT was used as the polycation while ALG and HA-DN acted as interspersed polyanions. Fresh polyelectrolyte solutions were prepared by dissolution of HA-DN, ALG and CHT in 0.15 M of NaCl to yield a final concentration of 0.25, 0.5 and 0.5 mg.mL⁻¹, respectively. The sensor crystals used were AT-cut quartz (Q-Sense) with gold plated polished electrodes. These crystals were excited at 5 MHz as well as at 15, 25, 35, 45 and 55 MHz corresponding to the 3rd, 5th, 7th, 9th and 11th overtones. The crystals were previously cleaned with sequential sonication for 3 min in acetone, ethanol and isopropanol and then dried with flowing nitrogen gas avoiding contamination prior to use. Firstly, the polyelectrolyte solutions were injected into the cell for 6 min, beginning with CHT. A rinsing step of 4 min with the solvent was included between the adsorptions of each polyelectrolyte. The multilayer systems were assembled at pH 5.5. The pH was adjusted with HCl or sodium hydroxide (NaOH, pellets, Fine Chemicals, Akzo Nobel Chemicals S.A., Mons, Belgium). CHT/ALG/CHT/HA films were also prepared for comparison. Films with 8 layers (2 tetralayers (TL)) were produced. All experiments were conducted at 25 °C. During the entire process $f\nu$ and D shifts were continuously recorded as a function of time.

The films' viscoelastic properties were investigated using the Voigt viscoelastic model implemented in the QTools software from Q-Sense. According with this model, a Simplex algorithm was used to find the minimum of the sum of the squares of the scaled errors between the experimental and model f and D values. Changes in resonant frequency and dissipation of the 5th, 7th and 9th overtone were fitted. The solvent viscosity selected was 1 mPa.s and a film density of 1 g.cm⁻³. The solvent density was varied between values from 1000 to 1045 kg.m⁻³ to minimize the total error (χ^2).

Freestanding Multilayer Membranes Production and Characterization

Production of the freestanding multilayer membranes—The production of the multilayer membranes was achieved using the LbL methodology with the help of a home-made dipping robot (see Figure S1). Polypropylene (PP) substrates were immersed in alternated polyelectrolyte solutions with a rinsing solution deposition between each polyelectrolyte. The rinsing solution used was a 0.15 M NaCl (pH = 5.5) and the polymer solutions were used at a concentration of 2 mg. mL⁻¹ for CHT and ALG and 0.5 mg. mL⁻¹ for the others. Deposition time of the polyelectrolytes was 6 min and 4 min for the rinsing solution.

In the end of 100 TL, two types of FS were produced (see Figure S1): multilayer membranes containing CHI, ALG and HA ([CHT/ALG/CHT/HA]₁₀₀) and multilayer membranes containing CHI, ALG and HA-DN with the same number of layers ([CHT/ALG/CHT/HA-DN]₁₀₀).

Scanning Electron Microscope (SEM)—The surface morphology of the samples was observed using a Hitachi S4100 (Tokyo, Japan) SEM. All samples were coated with a conductive layer of sputtered gold. The SEM micrographs were taken using an accelerating voltage of 15 kV and at different magnifications. For the cross-section observation, the freestanding membranes were immersed in liquid nitrogen and fractured. After that, the free fracture region was observed by SEM.

Water uptake—The water uptake ability of both type of freestanding multilayer membranes was studied by immersing previously weighed dry samples in a phosphate buffer saline (PBS, Sigma) solution. The FS samples were removed from immersion at pre-determined time points (t= 5 min, 15 min, 30 min, 1 h, 2 h, 3 h, 6h, 12 h, and 24 h) in which the excess solution was removed using filter paper, and the membranes were then immediately weighed using an analytical balance (Radwag Balances and Scales, Radom, Poland). The water uptake was calculated using Equation 1.

$$\text{Water uptake(\%)} = \frac{(m_x - m_i)}{m_i} \times 100 \quad \text{Equation 1}$$

Where, m_i is the dry mass of the sample and m_x is the hydrated mass of the sample at a given time point.

Mechanical tests: tensile behaviour—The tensile behavior of the freestanding multilayer membranes was evaluated using the mechanical testing machine Shimadzu MMT-101N (Shimadzu Scientific Instruments, Kyoto, Japan) with a load cell of 100 N. The produced FS were cut into rectangular samples (30 x 5 mm²) and immersed in a PBS solution overnight at 37°C. Tensile tests were carried out with a gauge length of 10 mm and a loading speed of 1mm.min⁻¹. Resulting stress-strain curves allowed to determine the Young's Modulus, ultimate tensile strength and maximum extension at rupture of both [CHT/ALG/CHT/HA]₁₀₀ and [CHT/ALG/CHT/HA-DN]₁₀₀ freestanding membranes.

Mechanical tests: adhesive behaviour—The adhesive properties of the produced [CHT/ALG/CHT/HA]₁₀₀ and [CHT/ALG/CHT/HA-DN]₁₀₀ freestanding membranes were evaluated using a single lap shear adhesion strength test adapted from ASTM D1002 42. Rectangular samples (30 x 10 mm²) were cut and overlapped in pairs with an overlapping area of 5 x 10 mm². Samples were then hydrated with a PBS solution and placed between firmly tight glass slides, overnight and at 37 °C. After that, the glass slides were removed and the samples were tested using the mechanical equipment Shimadzu MMT-101N, with each grip pulled the extremity of one of the overlapped samples. A tensile speed of 5 mm.min⁻¹ was used until sufficient stress was applied for membrane detachment. The

resulting stress-strain curves allowed to determine the adhesion strength of the [CHT/ALG/CHT/HA]₁₀₀ and the [CHT/ALG/CHT/HA-DN]₁₀₀ freestanding membranes.

Biofilm formation analysis—To evaluate the bactericidal activity of the membranes, *Staphylococcus aureus* was used as model of a gram-positive bacterium, whereas *Escherichia coli* used as model of a gram-negative bacterium. To do that, both strains of bacteria (1×10^8 Colony-forming unit (CFU) mL⁻¹) were grown in sterilized LB (Lysogeny broth) and incubated for 4h at 37°C. 200 µL of the bacterial suspension were placed on the LB agar growth plates and spread uniformly using a sterile cotton swab. The different sides of the membranes were placed on the top of the inoculated agar plates and incubated overnight at 37°C. To determine the biofilm formation at the membranes surface' and the bacterial growth, SEM images were acquired.

***In vitro* biological assays**

Human primary dermal fibroblasts (HDFs) were obtained from ATCC in partnership with LGC (USA) and used at passages between 8 and 11. The cells were cultured with DMEM (Gibco, ThermoFisher Scientific, Waltham, Massachusetts, United States of America) supplemented with 3.7 mg. mL⁻¹ sodium bicarbonate (Sigma), 10% fetal bovine serum (FBS, ThermoFisher Scientific), and 1% penicillin–streptomycin (Gibco) at pH 7.4. The cells were grown in 75 cm² tissue culture flasks and incubated at 37 °C in a humidified air atmosphere of 5% CO₂. The medium was changed every 3–4 days. When confluent, cells grown in tissue culture flasks were washed with Dulbecco's phosphate-buffered saline (DPBS, Corning, New York, United States of America) and subsequently detached by a chemical procedure with trypLE™ express solution (Life Technologies™) for 5 min at 37 °C in a humidified air atmosphere of 5% CO₂. To inactivate the trypLE™ express solution effect, cell culture medium was added. The cells were then centrifuged at 300 g and 25 °C for 5 min and the medium was decanted. Prior to cell seeding, the samples were disinfected by immersion in ethanol for 2 hs and then washed with DPBS. 300 µL of supplemented DMEM containing a cell suspension with 1×10^4 cells was dropped above the surface of the samples: [CHT/ALG/CHT/HA-DN]₁₀₀ membranes, the respective control [CHT/ALG/CHT/HA]₁₀₀ membranes and the positive control (tissue culture polystyrene substrates, TCPS) (in triplicate). Then, the samples were incubated at 37 °C in a humidified air atmosphere of 5% CO₂. After 4 hs, fresh culture medium was added.

[3-(4,5-dimethylthiazol-2-yl)-5-(3-carboxymethoxyphenyl)-2-(4-sulfophenyl)-2H-tetrazolium, inner salt (MTS) assay—The samples were tested for cytotoxicity using MTS (CellTiter 96® AQueous One Solution Cell Proliferation Assay, Promega, Madison, Wisconsin, USA) colorimetric assay. Briefly, the samples with adhered cells were placed in a non-treated surface 24-well cell culture plate (in triplicate) and incubated at 37 °C and 5% CO₂. At 1, 3 and 7 days of culture, the assay was performed, protected from light. The culture medium was removed and 500 µL of supplemented DMEM containing MTS solution with a dilution ratio of 1:5 was added to each well. Samples were then incubated in the dark at 37 °C and 5% CO₂. After 3 hs, 100 µL of each well (in triplicate) was transferred to a 96-well plate. The absorbance was monitored at 490 nm using a microplate reader Synergy HTX (BioTek Instruments, Inc., Winooski, Vermont, USA).

DNA quantification assay—A DNA quantification assay (Quant-iT™ PicoGreen® dsDNA Assay Kit, Invitrogen™, Thermo Fisher Scientific, Waltham, Massachusetts, USA) was performed to evaluate cell proliferation in the samples. For each culture time, the wells of the plate (the same samples used in viability assay) were extensively washed with DPBS, and then, 1 mL of ultrapure sterile water was added to each well. The well plate was placed in a shaking water bath at 37 °C for 1 h and then the content of each well was transferred for eppendorfs. Ultimately, the eppendorfs were immediately stored at –80 °C until use. The quantification of total DNA was determined after cell lysis, according to the manufacturer's description. After transferring each solution to a 96-well white opaque plate (in triplicates), the plate was incubated at room temperature and protected from light for 10 min. The standard curve for DNA analysis was generated with provided DNA from the assay kit. Fluorescence was read at excitation of 485/20 nm and emission of 528/20 nm using a microplate reader Synergy HTX.

Morphological observation of HDFs adhered on the freestanding multilayer membranes—Primary HDFs cell morphology was observed using a fluorescence microscope (Axio Imager 2, Zeiss, Oberkochen, Germany). Briefly, the cells were seeded above the samples (squares 1 cm²) at a density of 5×10^3 cells. cm⁻² and cultured for three and seven days, using basal culture conditions. After each time-point, the samples were gently washed with sterile DPBS and fixed with 10% (v/v) of formalin (Sigma) in DPBS solution for 30 min. To obtain morphological fluorescence images, rhodamine phalloidin (ThermoFisher Scientific) and 4',6-diamidino-2-phenylindole (DAPI, ThermoFisher Scientific) were used as fluorochromes. Rhodamine phalloidin stains F-actin while DAPI binds to AT regions of DNA, staining the cell nucleus. In the fluorescent assay, the fixed samples were initially permeabilized with 0.2% (v/v) of Triton X-100 (Sigma) in DPBS solution for 10 min and then blocked with 5% FBS (v/v) in DPBS solution for 30 min. Then, the samples were treated with rhodamine phalloidin for 45 min and subsequently with DAPI for 15 min. After this procedure, the cell morphology was observed using the fluorescence microscope.

***In vivo* biological assays**

All the animal experiments were performed according to the protocol approved by the Ethics Committee of Centro Hospitalar Cova da Beira (approval number 24/2009) and the guidelines set forth in the National Institute for the care and use of laboratory animals. To perform the *in vivo* assays, a total of 10 Wistar rats (4-6 weeks) weighing between 100- 150 g were used. The experimental setup was performed according to that previously used by Miguel S. *et al.* 43. Animals were separated into three groups: group 1, wounds were treated with [CHT/ALG/CHT/HA]₁₀₀ membrane; group 2, wounds were covered [CHT/ALG/CHT/HA-DN]₁₀₀ membrane; whereas in the group 3, used as control, wounds were covered with serum physiologic solution. During the study, animals were kept in separate cages and were fed with commercial rat food and water ad libitum. Animals were sacrificed after 10 and 21 days.

Hematoxilin and Eosin staining analysis—To evaluate the local and systemic immune response of different membranes, tissue specimens were obtained from each wound

area by sharp dissection at days 10 and 21. Skin tissue samples were obtained by necropsy, formalin fixed and paraffin embedded for histological processing. Sections of 3 μm were obtained from each sample using a cryostat microtome (Leica CM1900) and then stained with hematoxylin and eosin (H&E) or with Toluidine blue. Subsequently, samples were visualized using a light microscope with a specific image analysis software from Zeiss. Skin fragments without membrane were used as control. Other tissue samples such as brain, lung, liver, spleen and kidney, were also obtained by necropsy and analyzed to check for any morphological.

Statistical Analysis

All quantitative data was represented as average value \pm standard deviation with at least 5 replicates for each test subject, unless specifically mentioned. For tensile and lap shear strength adhesion data, an unpaired t test with Welch's correction was used. For the cellular assays, two-way ANOVA was used. Statistical significance of all tests was accepted for $p < 0.05$ (*). All statistical analysis was performed using the software GraphPad Prism 6.0.

Results

Synthesis and characterization of the conjugate HA-DN

HA is a component of the ECM, and may be combined with other polyelectrolytes to produce biocompatible and biodegradable materials to be applied as wound skin dressings⁴⁴. To provide an adhesive character to this material, HA was conjugated with DN, taking advantage of carbodiimide chemistry. UV-vis spectroscopy standard spectra were obtained from solutions with different concentrations of free DN and are represented in the inset of Figure S2, where it is possible to confirm the characteristic UV-excitation band of DN, centered at 280 nm. For DN concentrations less than 1.0 mM, the relation between DN concentration and absorbance followed a linear regime - Figure S2. UV- vis spectra of the HA and the conjugate HA-DN solution are presented in Figure 1. Besides confirming that the DN characteristic peak just appeared in the spectrum of the conjugate HA-DN, we also estimated the degree of DN substitution. Using the measured absorbance for the HA-DN, obtained at 280 nm, and the linear growth equation obtained from Figure 1A, the degree of DN substitution in the conjugate is 24%. Furthermore, the $^1\text{H-NMR}$ spectra of HA and HA-DN were acquired, see Figure S3.

Polyelectrolyte multilayers building-up

Prior to QCM-D monitoring, the ζ - potential of the different polyelectrolyte solutions was measured at working conditions (pH of 5.5 and ionic strength at 0.15 M). As expected, CHT presented a positive charge ($+19.8 \pm 1.3$ mV) while all the other polyelectrolyte solutions presented a negative charge. The ζ - potential values for ALG, HA and HA-DN solutions were -25.1 ± 2.4 mV, -26.7 ± 1.8 mV and -20.2 ± 1.7 mV, respectively.

Once the conjugate was prepared, the ability to construct the polyelectrolyte multilayers was followed *in situ* by QCM-D monitoring. Figures 2A and 2B show the variation of the normalized frequency (f/v) and dissipation (D) of the 5th overtone corresponding to the deposition of 2 CHT/ALG/CHT/HA-DN or CHT/ALG/CHT/HA tetralayers (TL) of

polyelectrolytes; Figure 2A corresponds to the control system with HA and Figure 2B corresponds to the system containing the conjugate HA-DN. The curves represent the state of frequency and dissipation after each material deposition which can be distinguished by the stepwise decrease in frequency and increase in dissipation. The decrease in frequency in each deposition step indicates that mass was adsorbed onto the gold-coated quartz crystals representing a successful deposition. The increase in dissipation values after each layer deposition indicates a non-rigid behavior of the materials adsorbed above the crystal's surface. The chemical nature of the used materials, the salt composition of the chosen solvent and washing buffer can have great influence on the viscoelastic nature of the resulting multilayer film 41. Usually, lower increase of D indicates that the film layer becomes denser than for higher increase of D . Moreover, the QCM-D data were used to estimate the thickness along with the film construction, as shown in Figure 2C. Assuming a viscoelastic film, the polymer layers were modelled as an elastic component in parallel with a viscous part 45, 46 – the Voigt Model. In result, both systems can be represented by a linear growth model during the construction of the first 8 layers. However, the overall estimated thickness for the [CHT/ALG/CHT/HA] system was smaller than for the [CHT/ALG/CHT/HA-DN].

Production and characterization of the freestanding polyelectrolyte multilayer membranes

QCM-D experiments confirmed the ability to deposit the chosen polyelectrolytes above a quartz crystal. A homemade dipping robot was used to produce freestanding multilayer membranes, by repeating the process 100 times over low surface energy substrates. In the end two freestanding membranes were obtained from the simple detachment of the multilayers by drying: [CHT/ALG/CHT/HA]₁₀₀ and [CHT/ALG/CHT/HA-DN]₁₀₀. All the necessary steps to produce the freestanding multilayer membranes are represented in Figure S1.

SEM—The morphology of the surface of the freestanding membranes was investigated by SEM. Figure 3A and 3B represent the morphology of the [CHT/ALG/CHT/HA]₁₀₀ surface's membrane at different magnifications; it was possible to observe a quite homogeneous morphology, presenting some micro features over the entire surface. The cross-section of the [CHT/ALG/CHT/HA]₁₀₀ – see Figure 3C- also appeared homogeneous along with the thickness. Figure 3D and 3E show the morphology of the [CHT/ALG/CHT/HA-DN]₁₀₀ surface's membrane at different magnifications; it was possible to observe some nano to microfeatures randomly distributed over the entire surface, together with a very porous and interconnected structure. Moreover, the cross-section of the [CHT/ALG/CHT/HA-DN]₁₀₀ is presented in Figure 3F, being less homogeneous than for the other system. Therefore, the thickness of both [CHT/ALG/CHT/HA]₁₀₀ and [CHT/ALG/CHT/HA-DN]₁₀₀ freestanding membranes was calculated from the cross-section images, being $18.7 \pm 1.22 \mu\text{m}$ for the control system and $25.3 \pm 1.10 \mu\text{m}$ for the DN-containing film.

Water uptake and tensile mechanical testing—The water uptake of the [CHT/ALG/CHT/HA]₁₀₀ and [CHT/ALG/CHT/HA-DN]₁₀₀ freestanding membranes was also evaluated for 1 day in PBS solution at 37 °C - see Figure 4A. Both membranes showed ability to uptake water molecules; [CHT/ALG/CHT/HA]₁₀₀ and [CHT/ALG/CHT/HA-

DN]₁₀₀ freestanding membranes seemed to reach the equilibrium after 1 h and 15 min in PBS, respectively. After these times, no significant changes occur in the system, in terms of water uptake. Comparing both systems, [CHT/ALG/CHT/HA]₁₀₀ freestanding membranes showed significant higher water content percentages than CHT/ALG/CHT/HA-DN]₁₀₀ membranes.

Tensile tests were also performed to study the mechanical properties of these materials – see Figure 4B, which show the most representative stress-strain curves for the [CHT/ALG/CHT/HA]₁₀₀ and [CHT/ALG/CHT/HA-DN]₁₀₀ freestanding membranes, respectively. From these, it was possible to calculate important parameters like the Young's modulus, the ultimate tensile strength and the maximum extension (Figure 4C) for each type of membrane. All parameters are higher for the [CHT/ALG/CHT/HA-DN]₁₀₀ than for the [CHT/ALG/CHT/HA]₁₀₀ freestanding membranes, with significant differences in terms of Young's modulus (8.3±1.47 MPa against 2.1±0.37 MPa) and ultimate tensile strength (1725.2±236.53 kPa against 654.3±125.19 kPa).

“Bioactivity” properties: from adhesiveness to bacteriostatic—For the last years cathecols have been widely investigated to enhance adhesive 47 and also bacteriostatic properties 48 of different materials. Therefore the assessment of the lap shear adhesion strength and anti- bacterial tests were performed on the produced membranes.

Briefly, the HA-DN or HA side of a rectangle part of the membrane was put in contact with the CHT side of other rectangle part of the membrane and left under pressure stimuli overnight. Then, the samples were subjected to adhesion tests where the required lap shear bonding strength necessary to detach the two parts of the systems was recorded– see Figure 4D. Therefore, we found that [CHT/ALG/CHT/HA]₁₀₀ required a lap shear adhesion strength of 1.1±0.2 MPa while [CHT/ALG/CHTD/HA-DN]₁₀₀ ones involved higher lap shear strength of about 2.0±0.2 MPa, as show in the graph of Figure 4E. It means that more strength was needed to detach the DN-containing freestanding membranes, allowing us to conclude that DN significantly contribute on enhancing the adhesive properties of the membranes.

Biofilm formation at the surface of the different materials was assessed by SEM. In Figure 5, it is possible to observe some bacteria at the surface of HA layer without DN and CHT layer, although their number is not enough to be considered a biofilm, for both strains. On the other hand, HA-DN showed an increased bacterial adhesion at its surface when in contact with *S. aureus* but the inverse happened for *E.coli.*, where it is possible to observe that HA-DN and CHT layer did not present enough bacteria to be considered a biofilm.

***In vitro* cell culture with HDFs**

HDF cells were cultured over both [CHT/ALG/CHT/HA]₁₀₀ and [CHT/ALG/CHT/HA-DN]₁₀₀ freestanding multilayers membranes for 7 days.

Cellular metabolic activity and cell content—The metabolic activity gave an indication about the cell viability and capability to proliferate – see Figure 6A. From the first day of culture significant differences ($p < 0.01$) were found between cells cultured over

[CHT/ALG/CHT/HA]₁₀₀ and [CHT/ALG/CHT/HA-DN]₁₀₀ freestanding multilayers, with the DN-containing membranes presenting higher values of metabolic activity. This trend was maintained at 3 and 7 days ($p < 0.001$), suggesting good cell viability and activity on the surface of catechol-containing membrane. A more accurate measurement of proliferation was done by DNA quantification - see Figure 6B. Overall, these results are in accordance with the ones obtained for the metabolic activity, with higher values of DNA content for [CHT/ALG/CHT/HA-DN]₁₀₀ freestanding multilayers. For the first day of culture, significant differences ($p < 0.01$) were already found between the different formulations, suggesting that more cells attached to the surface. For the third and the seventh day of culture, these differences were even more pronounced ($p < 0.001$).

Cell Morphology—The morphology of the HDFs when adhered above the freestanding membranes was also evaluated by phalloidin-DAPI staining – see Figure 7. After 1 day of culture, the cells adhered above the freestanding membranes presented a more rounded shape than when adhered above TCPS. Nevertheless, this round morphology was altered along the days of culture; after 3 and 7 days, the cells present a spread morphology with well-defined actin filamentous and a spindle-like shape, either for both type of freestanding membranes or TCPS. Curiously, the cells adhered above the [CHT/ALG/CHT/HA-DN]₁₀₀ freestanding multilayer membranes seemed to grow starting from an aggregated portion of cells that connect one with each other, resulting in an interconnected cell network. Even that, the cells seemed strongly adhered to the surface of the membrane unlike it happens with the cells adhered above the [CHT/ALG/CHT/HA]₁₀₀ freestanding membranes. After 7 days of culture, there are much less HDFs adhered above the surface and the ones that exist seemed poorly adhered to the surface. In terms of cell density, we observed again more cells adhered and distributed above the [CHT/ALG/CHT/HA-DN]₁₀₀ freestanding multilayer membranes than above the [CHT/ALG/CHT/HA]₁₀₀.

***In vivo* assay**

A Hematoxylin-Eosin (H&E) staining of the skin wound tissues was performed during each timepoint of the assay – see Figure 8A. A broad region of hyper-proliferative epithelial layer is a hallmark of the regenerating wound edge 49. Typically, during wound maturation, the epidermal region narrows until it gets re-established to its original appearance, i.e., a very thin layer.

Clearly, for the wound area covered with the freestanding membrane, the inflammatory process was quite exuberant, i.e., the presence of inflammatory cells was more abundant. However, the wound healing process progresses to the next phases and the fibroblast proliferation and dermis production were evident, after 21 days.

In groups 1 and 3, we could see an epidermal region with an appearance of a thin layer without epidermal annexes formation. Unlike, group 2 showed a thin epidermal layer as well as the establishment of epidermal papillae. Hence, we could observe that wounds treated with DN membranes were in an advanced stage of the healing process (please see table 1 for further information), after 21 days.

Additionally, a blue toluidine staining was used to highlight the presence of mastocyte cells, where their cytoplasm contains granules composed of heparin and histamine that become blue or violet stained- see Figure 8B 50. The results show that group 2 presented the higher level of inflammation compared to the other groups, as it displays a lot of mastocyte cells after 10 days. In fact, all groups, except the control, showed a lot of mastocyte cells, probably due to the presence of a foreign material in the organism. However, after 21 days, in group 2 the mastocytes population was significantly reduced, resulting on the highest decreasing of inflammation between the 10th and the 21st days, among the different samples (please see Figure 8C for more data). Such results highlight the potential of using DN impregnated on HA membranes.

Discussion

Being the biggest and most exposed tissue of the human body, skin is always on the light of defects, trauma or burns. Considerable efforts have been employed to develop ideal scaffolds for skin tissue engineering and medicine regenerative purposes, inclusive to promote skin wound healing 1, 2, 5. Nowadays, scientists are focused on mimicking the structure, composition, topography, mechanical properties and even the biological function of ECM to achieve better materials³. Herein, we identified some criteria that must be taken into account in skin substitute production: besides being easy to handle and apply to the wound site, it should provide vital barrier function with appropriate water flux and be readily adherent, presenting suitable physical and mechanical properties³. Therefore, we got inspiration on mussel's bonding abilities, to develop a conjugated polymer capable of adding adhesive properties to our material, modifying the HA backbones chains with the catecholamine DN, using a carbodiimide chemistry reaction. The UV-vis spectra for HA and HA-DN solutions showed that only the conjugate HA-DN presented the characteristic peak band of DN, at 280 nm (see Figure 1). In fact, we could also determinate the degree of DN substitution by preparing a standard curve of known concentration of free DN and then following their UV excitation curve (Figure S2). The obtained substitution degree was 24%. This value is higher than some similar substitutions already reported in literature, indicating a better performance of our chemical conjugation reaction⁵¹.

Both the results of UV-vis spectroscopy and ¹H-NMR confirmed that DN was presented in the conjugated HA-DN. Therefore, we believe that the chosen conditions were an adequate commitment between substitution and waste of material and would have a considerable impact on the adhesion properties of the resulting scaffold.

Additionally, this scaffold should undergo controlled degradation, be sterile, non-cytotoxic and evoke minimal inflammatory reactivity, while still being cost effective³. The size of the skin wounds can be variable; therefore, it is highly recommendable to have a scaffold which acts like a patch on the skin wound and that we could cut according with the size of the defect. LbL is a cost-effective technique to produce multilayer structured membranes for tissue engineering²⁰. QCM-D monitoring confirmed the construction of a film composed by CHT, ALG and HA-DN or HA at the surface of the quartz sensor. Several QCM-D monitoring studies have been done with CHT and ALG⁴⁵ and with CHT and HA⁵², but it is the first time that all polymers were combined. This fact is mainly related with the desired

degradation rate and offering more robustness for the developed material. When inside human body, HA is known by its fast degradation through the action of hyaluronidases 53; however, we aimed a scaffold that undergo a controlled degradation, thus, adding an inherently non-degradable polysaccharide as ALG, we hypothesize that we could increase the time of degradation. For both cases of study, corresponding to Figure 2A and 2B, each decrease on the f corresponds to the adsorption of the corresponding polymers; indeed, similar f were obtained after each polymer deposition, suggesting that similar masses of the different polymers were deposited. This fact can be related with the charge of the polymers: measured zeta potential values for these polyelectrolytes, at pH 5.5, are close in terms of absolute value, being expected also similar changes of f . Note that it has been suggested 54 that electrostatic-based depositions require appropriate charge balance. Curiously, each decrease in f was followed by a subsequent increase, due to the desorption of a small fraction of free polyelectrolyte during the washing step. Each polymer deposition was also followed by the D increase for both type of films. However, D for CHT was lower than for the other polymers, meaning that when the polycation was adsorbed the film layer became denser than for the other polymers 55. This observation can be associated with the highly water affinity of ALG and HA, which introduced softer layers to the system. In fact, HA is a hygroscopic material, having high ability of attracting water molecules from the surrounding environment 56; combining hygroscopic polymers with non-hygroscopic ones could lead to detrimental effects. Analyzing the QCM-D data, we hypothesize that after the deposition of the first layer of either HA or HA-DN there were some re-arrangements of the film structure, which result in the weak detection of the subsequent CHT layer deposition. This effect disappeared after first TL was constructed, indicating that the construction films were already more stable. Comparing both CHT/ALG/CHT/HA and CHT/ALG/CHT/HA-DN systems, the catechol-containing one generated highest absolute values of f . In fact, when the modification of carboxylic acid groups in HA with carbodiimide chemistry happens, the surface charge of the conjugated decreased, as shown by the ζ -potential values. As follows, the absolute ζ -potential values of CHT and HA-DN solutions became more alike, allowing higher f . This observation goes according with thickness estimation results that revealed that after the construction of 2 TL, CHT/ALG/CHT/HA-DN was thicker than CHT/ALG/CHT/HA film (Figure 2C). This goes oppositely to our previous results which revealed the formation of thinner films for CHT/HA-DN systems 51. Such disagreement can be related by the incorporation of ALG in the multilayer system, as well as the different polymer concentrations and proportions.

Accordingly, biomimetic, polysaccharide-based and transparent membranes containing catechol domains were successfully produced following the same methodology already reported by Caridade S.G. *et al.* 27. The integrity of these membranes was maintained even after the detachment process, see Figure S1. SEM images of the upper layer of [CHT/ALG/CHT/HA]₁₀₀ (Figure 3A and 3B) and [CHT/ALG/CHT/HA-DN]₁₀₀ (Figure 3D and 3E) freestanding membranes showed singular rough morphologies, presenting micro to nanofeatures on their surface. Usually, rougher surfaces are preferred for cells adhesion and proliferation rather than smooth surfaces, mainly because roughness increases the contact area between cells and material 3, 57, 58. Often, polysaccharide-based membranes' surface must be modified to increase their cellular performance. Therefore, using HA or HA-DN we

could overcome the need of a surface treatment, being a time and money-saving strategy. Besides presenting a rough surface, [CHT/ALG/CHT/HA-DN]₁₀₀ freestanding membranes also exhibit a very porous structure. In fact, interconnected porous networks are benefic for cell nutrition, oxygen delivery, proliferation and migration processes, as well as to support and guide tissue vascularization^{59, 60}.

Nonetheless, the increase on the porosity often compromises the mechanical properties of the scaffolds, diminishing their structural stability⁶¹. Therefore, it is important that the developed freestanding membranes have enough mechanical strength to maintain integrity until wound heals. The mechanical properties of native skin ECM vary according with different individual parameters like anatomic site, age or even genetics⁶². Uniaxial tensile tests revealed that both type of membranes exhibit strain-stiffening behavior (Figure 4B), as well as happens for skin tissue where collagen fibers rotate, align, and straighten in the direction of stretch until the point of failure^{62, 63}. [CHT/ALG/CHT/HA]₁₀₀ freestanding membranes displayed a Young's modulus significantly lower than [CHT/ALG/CHT/HA-DN]₁₀₀ ones (Figure 4C); Moreover, catechol-containing membranes presented significantly higher values of ultimate tensile strength (Figure 4C). Also, maximum extension can be an important parameter, but no significant differences were found between the two systems (Figure 4C); the introduction of the HA or of the conjugate HA-DN seems to increase the ability of the freestanding membranes to strain, comparing with unmodified CHT/ALG multilayer membranes²⁸. Mechanical properties can be correlated with the water uptake behavior of the [CHT/ALG/CHT/HA]₁₀₀ and [CHT/ALG/CHT/HA-DN]₁₀₀ membranes. Figure 4A shows that [CHT/ALG/CHT/HA]₁₀₀ multilayer membranes presented higher ability to retain water molecules and become more hydrated than [CHT/ALG/CHT/HA-DN]₁₀₀ membranes. Previous studies reported that a kind of plasticization phenomenon of water molecules in polysaccharides can increase the molecular mobility and decrease the stiffness of the membrane²⁸. This fact can explain the lowest value of elastic modulus in the case of the control membranes.

The conjugate HA-DN was already reported in literature by conferring more adhesive behavior to materials^{39, 40}. In fact, [CHT/ALG/CHT/HA-DN]₁₀₀ multilayer membranes presented a significantly higher value of lap shear adhesion strength than their control [CHT/ALG/CHT/HA]₁₀₀ multilayer membranes (Figure 4D and 4E). We hypothesize that the increase in the bonding force is related with the strong adhesion force of catechol groups in the modified HA. Our results matched with previous investigations. Park H-J. *et al.*⁶⁴ developed a bioinspired hydrogel composed by HA modified with catechol moieties which presented better results in terms of biocompatibility and tissue adhesiveness compared with photopolymerized HA hydrogels; however, the adhesive strength of these hydrogels was about 47.61 ± 36.12 kPa, that is much less than the ones found in this investigation. Neto A. I. *et al.*⁵¹ reported the development of adhesive CHT/HA-DN coatings above glass slides; even though, their system presented an adhesive shear strength about 2.32 ± 2.20 MPa, which is in accordance with the one achieved with our system. Note, that besides DN can oxidize spontaneously when exposed to the air, we believe that when coupled to HA, the conjugated became more stable than having just DN. In fact, Neto A. I.⁵¹ et al. compared the adhesive strength obtained before and after exposing to sodium periodate oxidizing agent and conclude that no significant changes were found. Carvalho A. L. *et al.*⁶⁵ also produced

mussel-inspired LbL coatings for orthopedic purposes, composed by CHT and HA-DN, but also including silver-doped bioactive glass nanoparticles. Besides authors confirmed the adhesive properties, they also performed microbiological assays, suggesting that coatings containing silver-doped nanoparticles displayed an antibacterial effect against *S. aureus* and *E. coli* cultures, two of the major causes of various human infections.

For skin wound healing, the evaluation of the biofilm formation at the surface of the scaffold is also highly recommended⁹. While *S. aureus* is responsible by causing skin and soft tissue infections, *E. coli* is the most common cause of urinary tract infections. As observed by Figure 5, *E. coli* and *S. aureus* were not able to form any biofilms at the surface of HA-DN films. Such preliminary result can be explained by the intrinsic bacteriostatic effect of catecholamines⁶⁶.

Once several desired properties were assembled in one material, *in vitro* and *in vivo* experiments comproved that [CHT/ALG/CHT/HA-DN]₁₀₀ multilayer membranes were effectively more suitable for skin wound healing than [CHT/ALG/CHT/HA]₁₀₀ ones. Parameters like HDFs viability, proliferation and infiltration (see Figure 6A and 6B and Figure 7) were favored when cells were culture above the catechol-containing multilayer membranes, which imply that [CHT/ALG/CHT/HA-DN]₁₀₀ membranes were more functionally active than their control without DN. The main reasons for this improved behavior can be related with different aspects of the material. As above referred, rough and porous surfaces are usually described to enhance cellular behavior. Min B-M. *et al.*⁶⁷ produced silk fibroin nanofibers using electrospinning technology; the wide range of pore size distribution, the high porosity as well as the consequent high surface area to volume ratio of the nanofibers were suggested as favorable for cell adhesion, growth and proliferation. Also, Silva J. M. *et al.*⁶⁸ combined LbL with spherical template leaching to produce 3-dimensional nanostructures with high porosity and interconnectivity, just composed by self-assembled multilayers of CHT and chondroitin sulfate, to enhance cell adhesion and proliferation. Therefore, we hypothesized that it became easier for HDFs located on surface of the material to migrate into the pores network, due to the high porosity that [CHT/ALG/CHT/HA-DN]₁₀₀ multilayer membranes could offer for cell infiltration and growth. On the other hand, the stiffness of the material has been often referred as capable of modulating the cellular behavior above the material's surface. Ren K. *et al.*⁶⁹ produced poly(L-lysine)/hyaluronan multilayer films of controlled stiffness to evaluate the influence of this parameter on cellular behavior; they concluded that stiff films enhanced proliferation whereas soft films were not favorable for cell adhesion, spreading or proliferation. Our results are in agreement with this investigation: [CHT/ALG/CHT/HA-DN]₁₀₀ multilayer membranes were stiffer than the controls without DN, retaining less water volumes and increasing protein adsorption phenomena. Finally, the adhesive moieties conferred by DN have been also reported in literature to confer cell-adhesive properties. Yang X. *et al.*⁷⁰ conjugated recombinant human gelatin with DN to create biologically adhesive surfaces; they reported that the introduction of DN enhanced the binding of collagen-binding vascular endothelial growth factor and cell adhesion as compared with gelatin alone. Han L. *et al.*⁷¹ developed adhesive and tough polydopamine-clay-polyacrylamide hydrogels that favored cell attachment and proliferation, owing to the high cell affinity of polydopamine. We believe that more than mechanical adhesion, the introduction of DN on our freestanding

multilayer membranes' system conferred bioadhesive properties to the surface of the membrane unlike what happens to [CHT/ALG/CHT/HA]₁₀₀ multilayer membranes.

A complex *in vivo* wound healing process begins upon injury and includes different phases as blood clotting, inflammation, re-epithelialization, granulation tissue formation and tissue remodeling 72. Among other cell types, mastocytes have been reported to usually migrate to the inflammation site. Moreover, mastocytes increased population is proportional to the degree of inflammation of the lesion 73. In the inflammation phase, mastocyte cells accumulate at the wound site and release histamine, interleukins (IL-6 and IL-8), and growth factors such as vascular endothelial growth factor (VEGF) 74. Posteriorly, mastocytes release serine proteases (chymase and tryptase), that breakdown the ECM inducing proliferation of fibroblasts and endothelial cells, initiating the following phase of wound healing process. Furthermore, the infiltration of neutrophils and other inflammatory mediators is enabled through vasodilatation and increased vascular permeability 75. Reduction of inflammation process was more evident after 21 days for [CHT/ALG/CHT/HA-DN]₁₀₀ multilayer membranes. DN has been reported to reduce inflammation by inducing upregulation of cytokines, chemokines, adhesion molecules and by producing anti-inflammatory mediators 51, 75. The control group (group 3) as well as [CHT/ALG/CHT/HA]₁₀₀ multilayer membranes (group 1) were not able to reduce the mastocytes population. Hence, we hypothesize that the cells could populate the surface of the DN-containing membranes which is more porous, stiffer and adhesive than the [CHT/ALG/CHT/HA]₁₀₀ membrane, building up a scaffold that enhances skin tissue engineering. Moreover, we believe that the porosity of the surface of the [CHT/ALG/CHT/HA-DN]₁₀₀ multilayer membranes could increase the cellular ingrowth, which could mimic even better the features of native ECM.

Overall, we could produce adhesive and biomimetic multilayer membranes, composed by natural-based materials, that could act as patch to replace the functions of native ECM until host cells can repopulate and resynthesize a new ECM for skin wound healing.

Conclusions

We constructed adhesive and bioinspired freestanding multilayer membranes, composed of polysaccharides, which morphology and composition recapitulate aspects presented by native ECM. The presence of DN, which contains catechol groups that were found as responsible for the adhesive behavior of mussels on wetted rocks, brought new advantages for this LbL system. The [CHT/ALG/CHT/HA-DN]₁₀₀ freestanding multilayer membranes supported better cell adhesion and proliferation and provided directional cues for cells communicate with each other and growth. These natural, biocompatible, highly porous and adhesive materials hold great potential in providing a support for skin wound healing, as shown by *in vitro* and *in vivo* assays.

Supplementary Material

Refer to Web version on PubMed Central for supplementary material.

Acknowledgements

M.P.S. acknowledges the Portuguese Foundation for Science and Technology (FCT) for financial support through Grant No. SFRH/BD/97606/2013. This work was supported by the European Research Council grant agreement ERC-2014-ADG-669858 for the ATLAS project. The authors acknowledge Paula Marques (Mechanical Engineering Department, University of Aveiro, Aveiro, Portugal) for providing the mechanical equipment to carry out the tensile tests and the lap shear adhesion tests.

References

1. Metcalfe AD, Ferguson MWJ. *Journal of the Royal Society Interface*. 2007; 4:413–437.
2. Chen M, Przyborowski M, Berthiaume F. *Critical reviews in biomedical engineering*. 2009; 37:399–421. [PubMed: 20528733]
3. Zhong SP, Zhang YZ, Lim CT. *Wiley Interdisciplinary Reviews: Nanomedicine and Nanobiotechnology*. 2010; 2:510–525. [PubMed: 20607703]
4. Herndon DN, Barrow RE, Rutan RL, Rutan TC, Desai MH, Abston S. *Annals of surgery*. 1989; 209:547–552. [PubMed: 2650643]
5. Andersson, LC, Nettelblad, HC, Kratz, G. *Artificial Organs*. Hakim, NS, editor. Springer London; London: 2009. 93–105.
6. Tenenhaus M, Rennekampff HO. *Plastic and reconstructive surgery*. 2016; 138:42s–50s. [PubMed: 27556774]
7. Langer R, Vacanti J. *Science*. 1993; 260:920–926. [PubMed: 8493529]
8. Skorkowska-Telichowska K, Czemplik M, Kulma A, Szopa J. *Journal of the American Academy of Dermatology*. 2013; 68:e117–126. [PubMed: 21982060]
9. Sood A, Granick MS, Tomaselli NL. *Advances in Wound Care*. 2014; 3:511–529. [PubMed: 25126472]
10. Caravaggi C, De Giglio R, Pritelli C, Sommara M, Dalla Noce A, Faglia E, Mantero M, Clerici G, Fratino P, Dalla Paola L, Mariani G, et al. A prospective, multicenter, controlled, randomized clinical trial. 2003; 26:2853–2859.
11. Dantzer E, Braye FM. *British journal of plastic surgery*. 2001; 54:659–664. [PubMed: 11728107]
12. Norouzi M, Boroujeni SM, Omidvarkordshouli N, Soleimani M. *Advanced healthcare materials*. 2015; 4:1114–1133. [PubMed: 25721694]
13. Hou Q, Grijpma DW, Feijen J. *Biomaterials*. 2003; 24:1937–1947. [PubMed: 12615484]
14. Sun G, Zhang X, Shen YI, Sebastian R, Dickinson LE, Fox-Talbot K, Reinblatt M, Steenbergen C, Harmon JW, Gerecht S. *Proceedings of the National Academy of Sciences of the United States of America*. 2011; 108:20976–20981. [PubMed: 22171002]
15. Jaiswal M, Gupta A, Agrawal AK, Jassal M, Dinda AK, Koul V. *Journal of biomedical nanotechnology*. 2013; 9:1495–1508. [PubMed: 23980498]
16. Hong Y, Chen X, Jing X, Fan H, Gu Z, Zhang X. *Advanced Functional Materials*. 2010; 20:1503–1510.
17. Cao H, Chen MM, Liu Y, Liu YY, Huang YQ, Wang JH, Chen JD, Zhang QQ. *Colloids and surfaces. B, Biointerfaces*. 2015; 136:1098–1106. [PubMed: 26618451]
18. Chaudhari AA, Vig K, Baganizi DR, Sahu R, Dixit S, Dennis V, Singh SR, Pillai SR. *International Journal of Molecular Sciences*. 2016; 17:1974.
19. Borges J, Mano JF. *Chemical Reviews*. 2014; 114:8883–8942. [PubMed: 25138984]
20. Costa RR, Mano JF. *Chemical Society Reviews*. 2014; 43:3453–3479. [PubMed: 24549278]
21. Richardson JJ, Cui J, Björnmalm M, Braunger JA, Ejima H, Caruso F. *Chemical Reviews*. 2016; 116:14828–14867. [PubMed: 27960272]
22. Guthrie KM, Agarwal A, Teixeira LBC, Dubielzig RR, Abbott NL, Murphy CJ, Singh H, McAnulty JF, Schurr MJ. *Journal of burn care & research : official publication of the American Burn Association*. 2013; 34:e359–e367. [PubMed: 23511285]
23. Picart, C, Caruso, F, Voegel, JC, Decher, G. *Layer-by-Layer Films for Biomedical Applications*. Wiley; 2014.

24. Correia CR, Pirraco RP, Cerqueira MT, Marques AP, Reis RL, Mano JF. *Scientific Reports*. 2016; 6
25. Kulygin O, Price AD, Chong SF, Stadler B, Zelikin AN, Caruso F. *Small*. 2010; 6:1558–1564. [PubMed: 20578114]
26. Silva JM, Duarte ARC, Custódio CA, Sher P, Neto AI, Pinho ACM, Fonseca J, Reis RL, Mano JF. *Advanced healthcare materials*. 2014; 3:433–440. [PubMed: 23983205]
27. Caridade SG, Monge C, Gilde F, Boudou T, Mano JF, Picart C. *Biomacromolecules*. 2013; 14:1653–1660. [PubMed: 23590116]
28. Silva JM, Duarte AR, Caridade SG, Picart C, Reis RL, Mano JF. *Biomacromolecules*. 2014; 15:3817–3826. [PubMed: 25244323]
29. Mamedov AA, Kotov NA. *Langmuir*. 2000; 16:5530–5533.
30. Picart C, Elkaim R, Richert L, Audoin F, Arntz Y, Da Silva Cardoso M, Schaaf P, Voegel JC, Frisch B. *Advanced Functional Materials*. 2005; 15:83–94.
31. Salloum DS, Olenych SG, Keller TC, Schlenoff JB. *Biomacromolecules*. 2005; 6:161–167. [PubMed: 15638516]
32. Sousa MP, Caridade SG, Mano JF. *Advanced healthcare materials*. 2017; 6
33. Chrzanowski W, Khademhosseini A. *Advanced drug delivery reviews*. 2013; 65:403–404. [PubMed: 23500192]
34. Huang R, Li WZ, Lv XX, Lei ZJ, Bian YQ, Deng HB, Wang HJ, Li JQ, Li XY. *Biomaterials*. 2015; 53:58–75. [PubMed: 25890707]
35. Flammang P, Santos R. *Interface Focus*. 2015; 5
36. Lee H, Lee BP, Messersmith PB. *Nature*. 2007; 448:338. [PubMed: 17637666]
37. Lee BP, Messersmith PB, Israelachvili JN, Waite JH. *Annual review of materials research*. 2011; 41:99–132.
38. Ryu JH, Lee Y, Kong WH, Kim TG, Park TG, Lee H. *Biomacromolecules*. 2011; 12:2653–2659. [PubMed: 21599012]
39. Hong S, Yang K, Kang B, Lee C, Song IT, Byun E, Park KI, Cho S-W, Lee H. *Advanced Functional Materials*. 2013; 23:1774–1780.
40. Neto AI, Vasconcelos NL, Oliveira SM, Ruiz-Molina D, Mano JF. *Advanced Functional Materials*. 2016; 26:2745–2755.
41. Mano JF. *Macromolecular bioscience*. 2008; 8:69–76. [PubMed: 17902189]
42. ASTM. *Journal*. 1999
43. Miguel SP, Ribeiro MP, Brancal H, Coutinho P, Correia IJ. *Carbohydrate polymers*. 2014; 111:366–373. [PubMed: 25037363]
44. Croisier F, Atanasova G, Poumay Y, Jérôme C. *Advanced healthcare materials*. 2014; 3:2032–2039. [PubMed: 25263074]
45. Alves NM, Picart C, Mano JF. *Macromolecular bioscience*. 2009; 9:776–785. [PubMed: 19340816]
46. Dunér G, Thormann E, Dinait A. *Journal of Colloid and Interface Science*. 2013; 408:229–234. [PubMed: 23932084]
47. Sedó J, Saiz-Poseu J, Busqué F, Ruiz-Molina D. *Advanced Materials*. 2013; 25:653–701. [PubMed: 23180685]
48. Iqbal Z, Lai EPC, Avis TJ. *Journal of Materials Chemistry*. 2012; 22:21608–21612.
49. Silva RM, Silva GA, Coutinho OP, Mano JF, Reis RL. *Journal of Materials Science-Materials in Medicine*. 2004; 15:1105–1112. [PubMed: 15516871]
50. Donot F, Fontana A, Baccou JC, Schorr-Galindo S. *Carbohydrate Polymers*. 2012; 87:951.
51. Neto AI, Cibrão A, Correia CR, Carvalho RR, Luz G, Ferrer GG, Botelho G, Picart C, Alves NM, Mano JF. *Small*. 2014; 10:2459–2469. [PubMed: 24616168]
52. Neto AI, Cibrão AC, Correia CR, Carvalho RR, Luz GM, Ferrer GG, Botelho G, Picart C, Alves NM, Mano JF. *Small*. 2014; 10:2459–2469. [PubMed: 24616168]
53. Zhong SP, Campoccia D, Doherty PJ, Williams RL, Benedetti L, Williams DF. *Biomaterials*. 1994; 15:359–365. [PubMed: 8061127]

54. Fischer P, Laschewsky A, Wischerhoff E, Arys X, Jonas A, Legras R. *Macromolecular Symposia*. 1999; 137:1–24.
55. Slavin S, Soeriyadi AH, Voorhaar L, Whittaker MR, Becer CR, Boyer C, Davis TP, Haddleton DM. *Soft Matter*. 2012; 8:118–128.
56. Hargittai I, Hargittai M. *Structural Chemistry*. 2008; 19:697–717.
57. Chang, H-I, Wang, Y. *Regenerative Medicine and Tissue Engineering - Cells and Biomaterials*. Eberli, D, editor. InTech; Rijeka: 2011. Ch. 27
58. Silva SS, Popa EG, Gomes ME, Cerqueira M, Marques AP, Caridade SG, Teixeira P, Sousa C, Mano JF, Reis RL. *Acta Biomaterialia*. 2013; 9:6790–6797. [PubMed: 23462554]
59. Hajicharalambous CS, Lichter J, Hix WT, Swierczewska M, Rubner MF, Rajagopalan P. *Biomaterials*. 2009; 30:4029–4036. [PubMed: 19446874]
60. Rnjak-Kovacina J, Wise SG, Li Z, Maitz PKM, Young CJ, Wang Y, Weiss AS. *Biomaterials*. 2011; 32:6729–6736. [PubMed: 21683438]
61. Loh QL, Choong C. *Tissue Engineering. Part B, Reviews*. 2013; 19:485–502. [PubMed: 23672709]
62. Sander EA, Lynch KA, Boyce ST. *Journal of biomechanical engineering*. 2014; 136:051008. [PubMed: 24356985]
63. Yang W, Sherman VR, Gludovatz B, Schaible E, Stewart P, Ritchie RO, Meyers MA. *Nature Communications*. 2015; 6
64. Park H-J, Jin Y, Shin J, Yang K, Lee C, Yang HS, Cho S-W. *Biomacromolecules*. 2016; 17:1939–1948. [PubMed: 27112904]
65. Carvalho AL, Vale AC, Sousa MP, Barbosa AM, Torrado E, Mano JF, Alves NM. *Journal of Materials Chemistry B*. 2016; 4:5385–5393.
66. Dhand C, Harini S, Venkatesh M, Dwivedi N, Ng A, Liu S, Verma NK, Ramakrishna S, Beuerman RW, Loh XJ, Lakshminarayanan R. *ACS Applied Materials & Interfaces*. 2016; 8:1220–1232. [PubMed: 26709441]
67. Min BM, Lee G, Kim SH, Nam YS, Lee TS, Park WH. *Biomaterials*. 2004; 25:1289–1297. [PubMed: 14643603]
68. Silva JM, Georgi N, Costa R, Sher P, Reis RL, Van Blitterswijk CA, Karperien M, Mano JF. *PLOS ONE*. 2013; 8:e55451. [PubMed: 23437056]
69. Ren K, Crouzier T, Roy C, Picart C. *Advanced functional materials*. 2008; 18:1378–1389. [PubMed: 18841249]
70. Yang X, Zhu L, Tada S, Zhou D, Kitajima T, Isoshima T, Yoshida Y, Nakamura M, Yan W, Ito Y. *International Journal of Nanomedicine*. 2014; 9:2753–2765. [PubMed: 24920909]
71. Han L, Lu X, Liu K, Wang K, Fang L, Weng L-T, Zhang H, Tang Y, Ren F, Zhao C, Sun G, et al. *ACS Nano*. 2017; 11:2561–2574. [PubMed: 28245107]
72. Reinke JM, Sorg H. *European surgical research. Europäische chirurgische Forschung. Recherches chirurgicales europeennes*. 2012; 49:35–43. [PubMed: 22797712]
73. Alves NM, Gómez Ribelles JL, Gómez Tejedor JA, Mano JF. *Macromolecules*. 2004:3735–3744.
74. Sima F, Mutlu EC, Eroglu MS, Sima LE, Serban N, Ristoscu C, Petrescu SM, Oner ET, Mihailescu IN. *Biomacromolecules*. 2011; 12:2251–2256. [PubMed: 21520921]
75. Costa RR, Neto AI, Calgeris I, Correia CR, Pinho ACMd, Fonseca JC, Öner ET, Mano JF. *Journal of Materials Chemistry B*. 2013; 1:2367–2374.

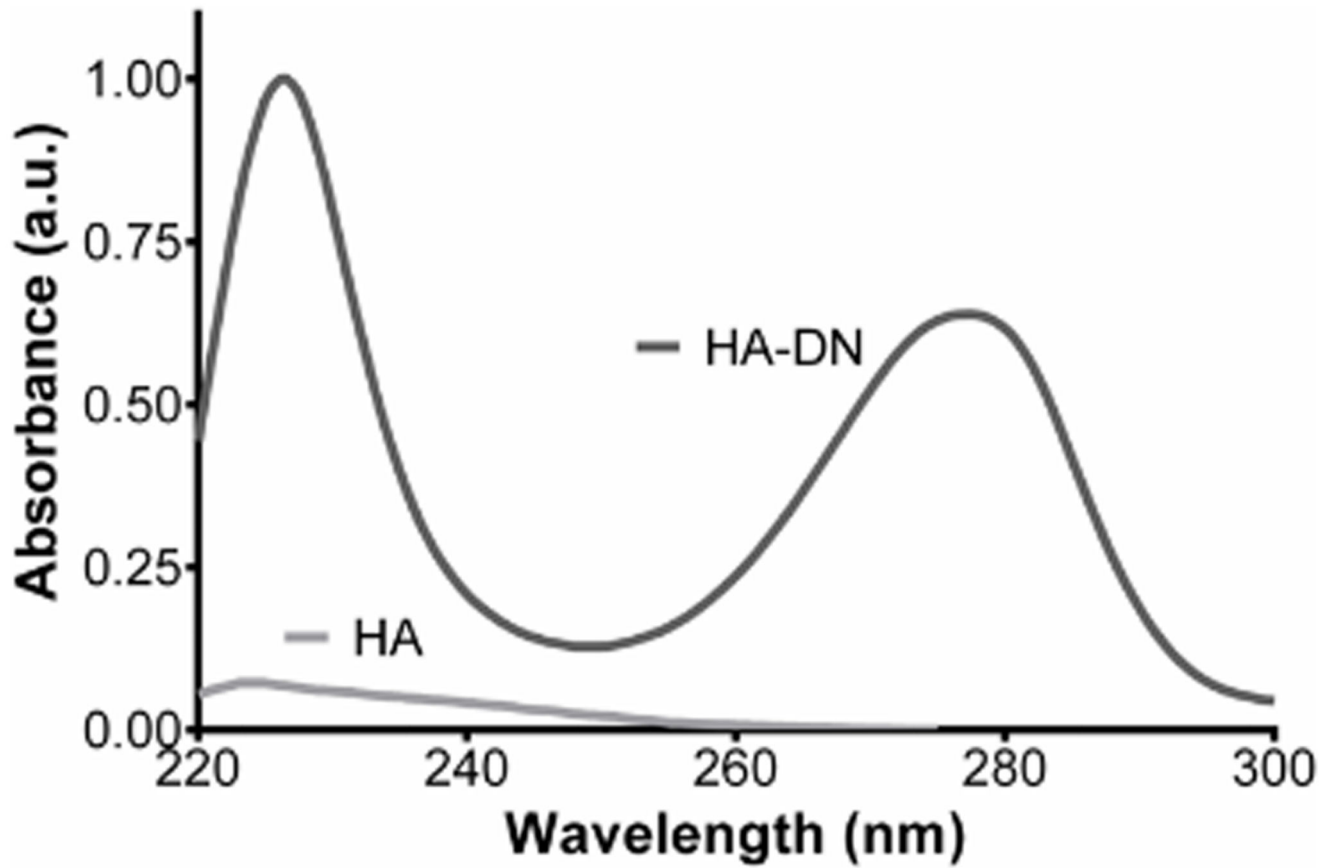


Figure 1. UV-vis spectra of the conjugate the conjugate (HA-DN) and the control (HA), which is also shown for comparison.

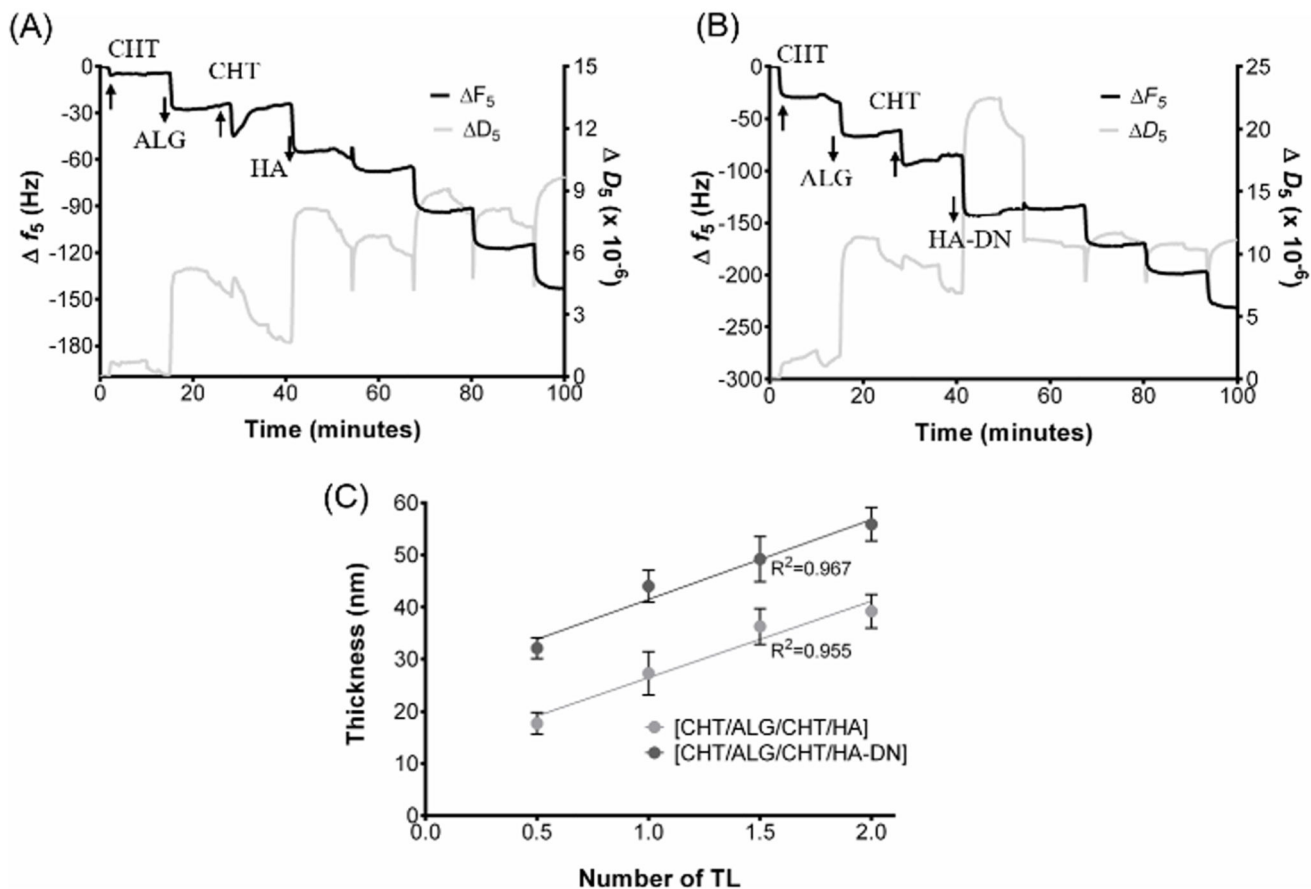


Figure 2. Build-up assemblies of A) chitosan (CHT), alginate (ALG) and hyaluronic acid (HA) and B) chitosan (CHT), alginate (ALG) and conjugate (HA-DN) up to 8 deposition layers (2 tetralayers) in 0.15 M of NaCl, using QCM-D monitoring. C) Cumulative thickness evolution of CHT/ALG/CHT/HA and CHT/ALG/CHT/HA-DN polymeric films as a function of the number of deposition tetralayers. Thickness measurements were estimated using a Voigt viscoelastic model. Both systems followed a linear trend, which are also represented in the graph.

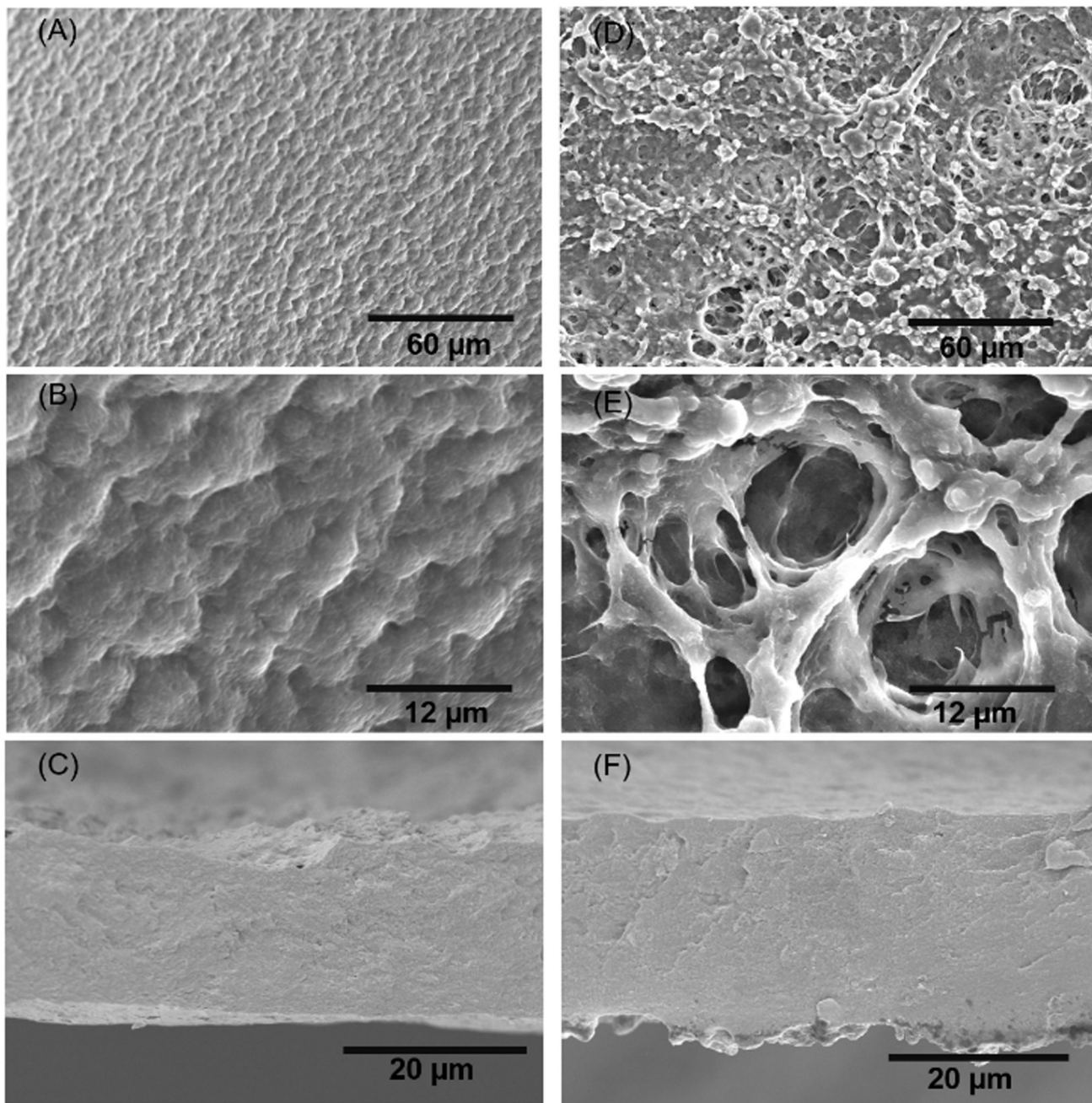
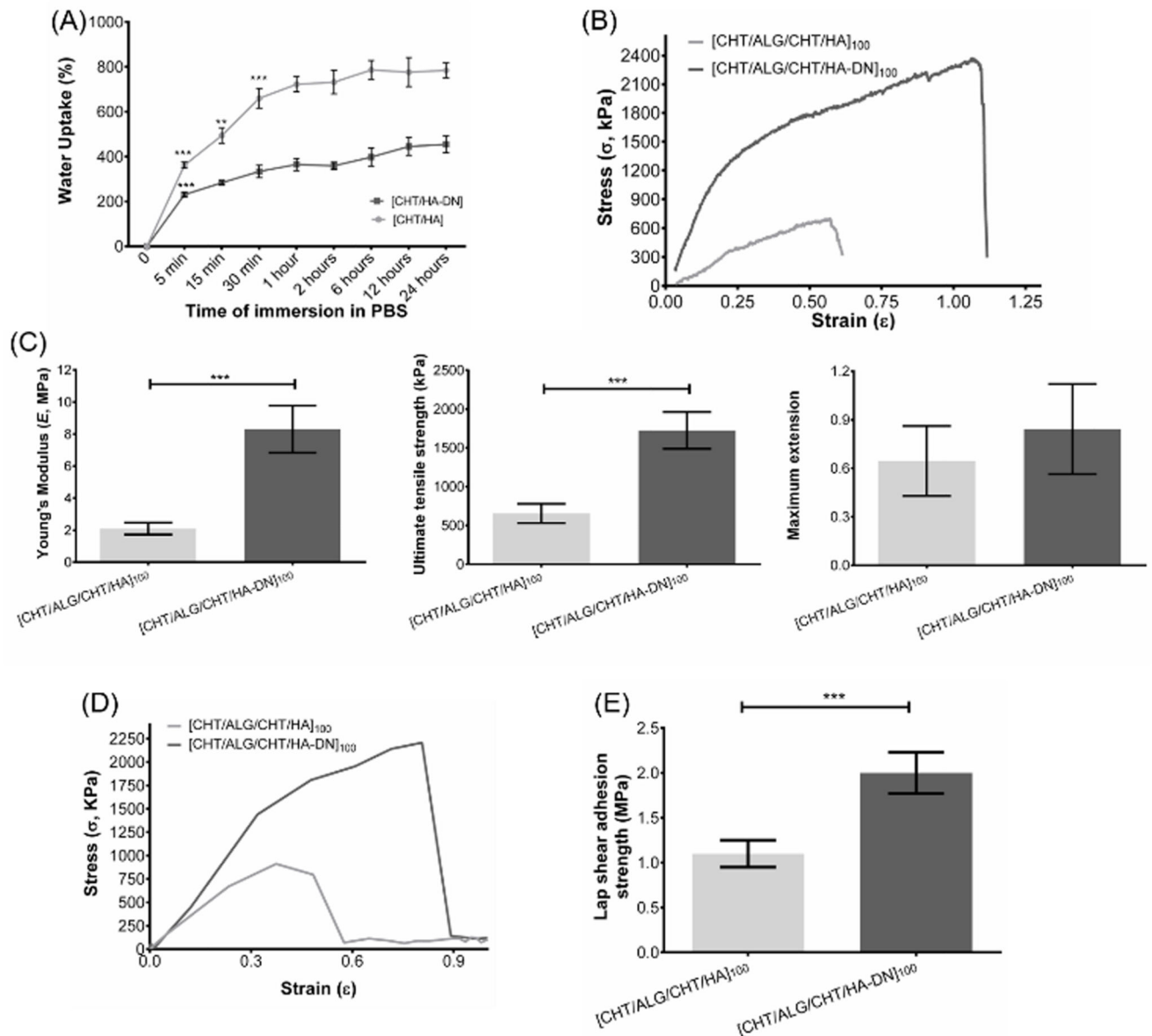


Figure 3. SEM images of the morphology of the upper side of the $[\text{CHI}/\text{ALG}/\text{CHI}/\text{HA}]_{100}$ at A) lower and B) higher magnifications. The cross-section of the $[\text{CHI}/\text{ALG}/\text{CHI}/\text{HA}]_{100}$ membrane is presented in C). SEM images of the morphology of the upper side of the $[\text{CHI}/\text{ALG}/\text{CHI}/\text{HA-DN}]_{100}$ at D) lower and E) higher magnifications. The cross-section of the $[\text{CHI}/\text{ALG}/\text{CHI}/\text{HA-DN}]_{100}$ membrane is depicted in F).

**Figure 4.**

A) Water uptake measurements of the [CHI/ALG/CHI/HA]₁₀₀ and [CHI/ALG/CHI/HA-DN]₁₀₀ freestanding multilayer membranes. B) Representation of a stress-strain curve, during the tensile tests, for [CHI/ALG/CHI/HA]₁₀₀ and [CHI/ALG/CHI/HA-DN]₁₀₀ hydrated membranes. Representation of the mechanical properties of the FS evaluated by tensile tests: C) Young's Modulus, ultimate tensile strength and maximum extension at rupture. D) Representative stress-strain curves, during the lap shear adhesion strength, for [CHI/ALG/CHI/HA]₁₀₀ and [CHI/ALG/CHI/HA-DN]₁₀₀ glued hydrated membranes. E) Lap shear strength tests for both [CHI/ALG/CHI/HA]₁₀₀ and [CHI/ALG/CHI/HA-DN]₁₀₀ membranes. Data is presented as average ± standard deviation where significant differences were found for $p < 0.001$ (***) and $p < 0.01$ (**).

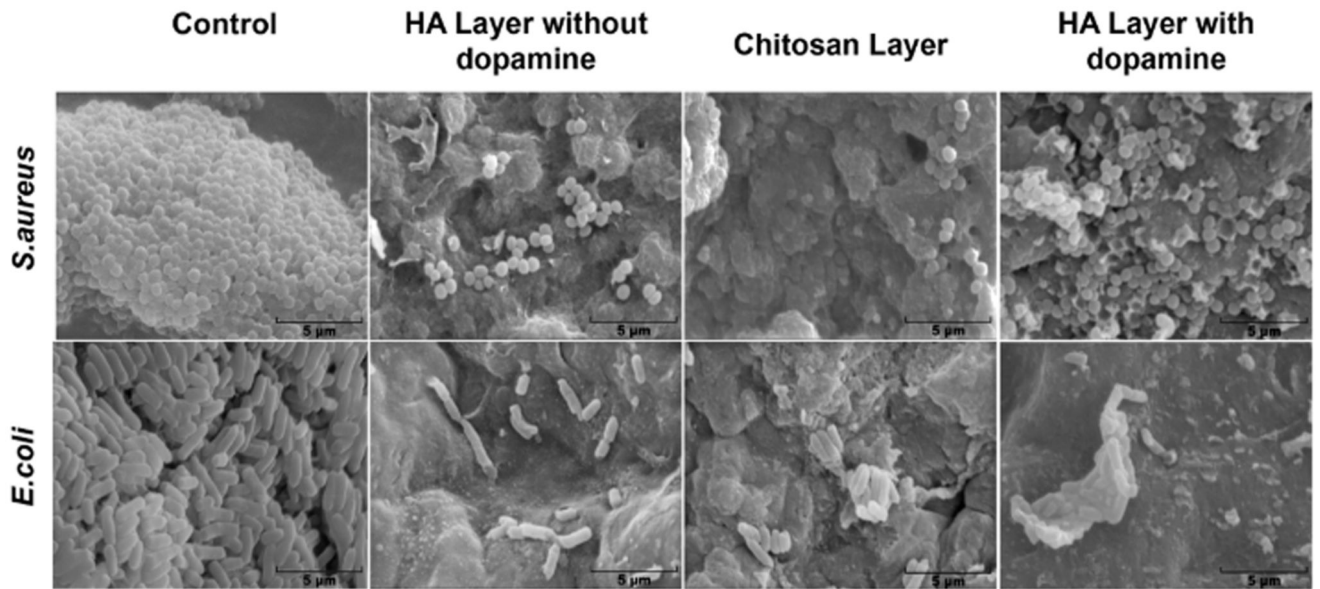


Figure 5. SEM images of biofilm formation for *S. aureus* and *E. coli* at the surface of the HA layer, CHT layer and HA-DN layer.

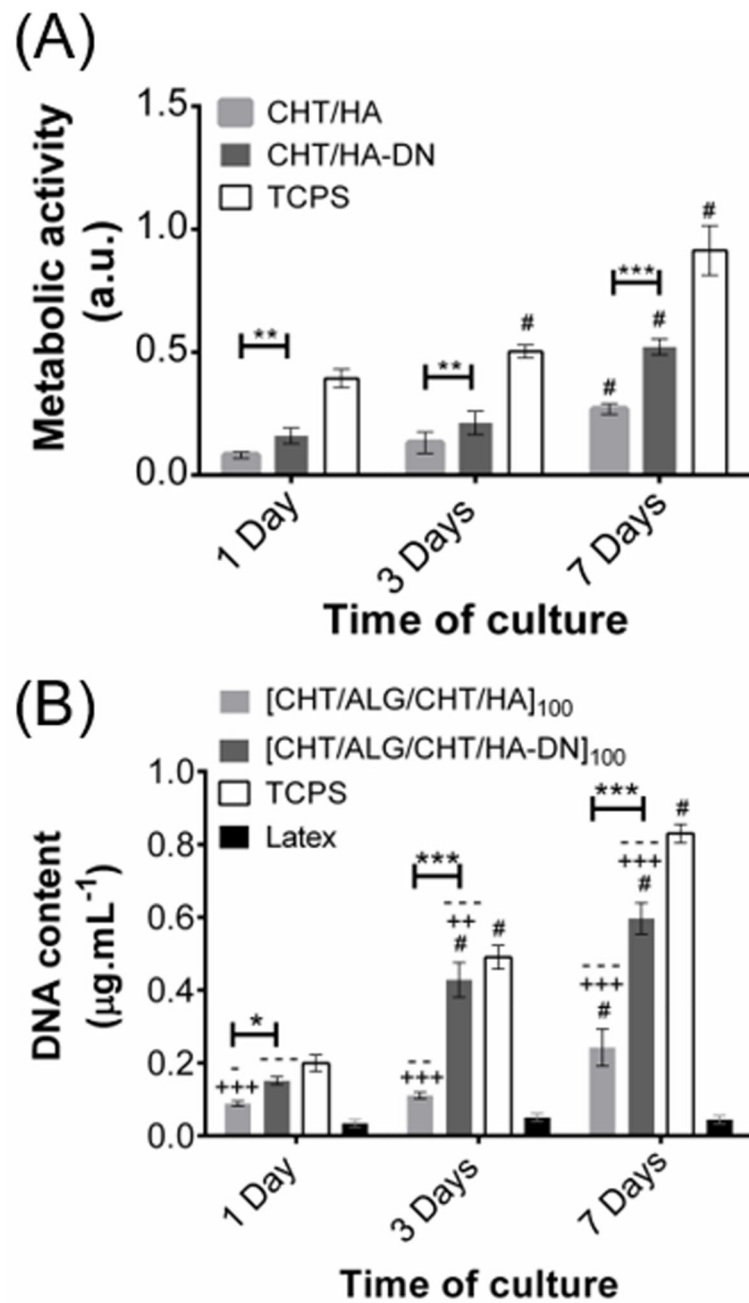


Figure 6.

A) Metabolic activity through the absorbance of HDFs seeded above the freestanding membranes (MTS assay) and B) cellular proliferation through the determination of the DNA content (DNA quantification assay), both for 1, 3 and 7 days. TCPS was used as positive control and latex as negative control. Significant differences were found for $p > 0.05$ (*); $p > 0.01$ (**) and $p > 0.001$ (***), between the membranes' systems. Moreover, significant differences with the positive control TCPS were found for $p > 0.01$ (++) and $p > 0.001$ (+++)

and with negative control latex for $p > 0.05$ (-); $p > 0.01$ (--) and $p > 0.001$ (---). Significant differences with each previous time points were found for $p < 0.001$ (#).

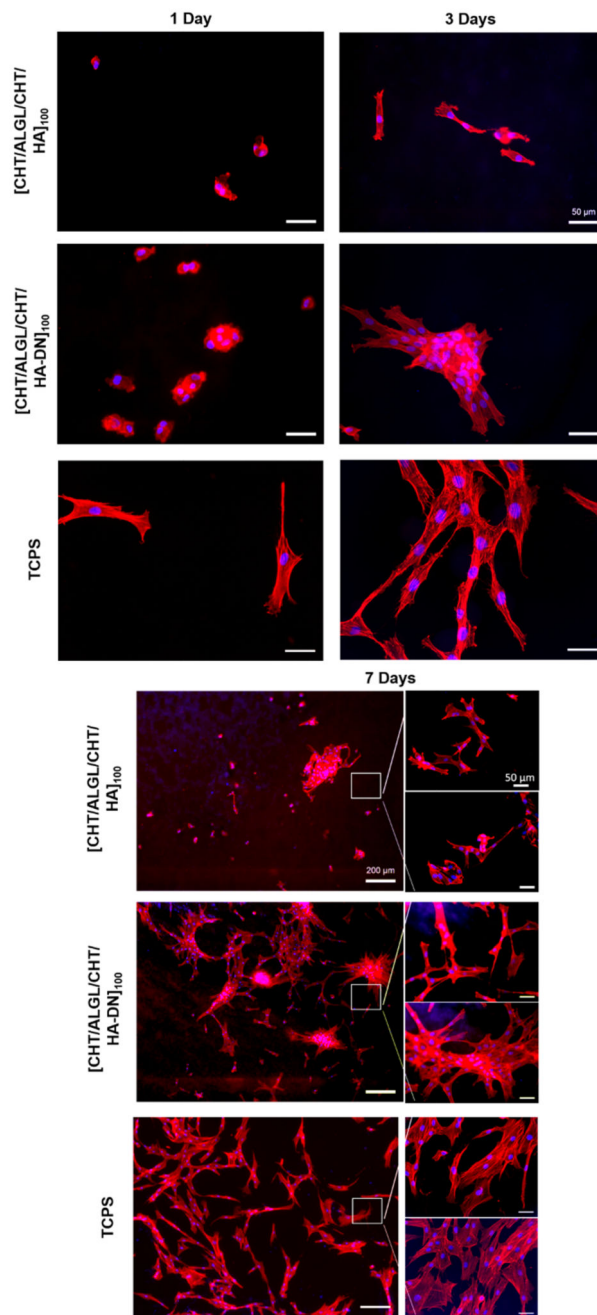


Figure 7.

Representative images of HDFs cells over the $[\text{CHT}/\text{ALG}/\text{CHT}/\text{HA}]_{100}$ and $[\text{CHT}/\text{ALG}/\text{CHT}/\text{HA-DN}]_{100}$ membranes, represented by DAPI–phalloidin fluorescence assay at 1, 3 and 7 days. Cells nuclei are stained in blue by DAPI and F-actin filaments are stained in red by phalloidin. The scale bar is representative for all images.

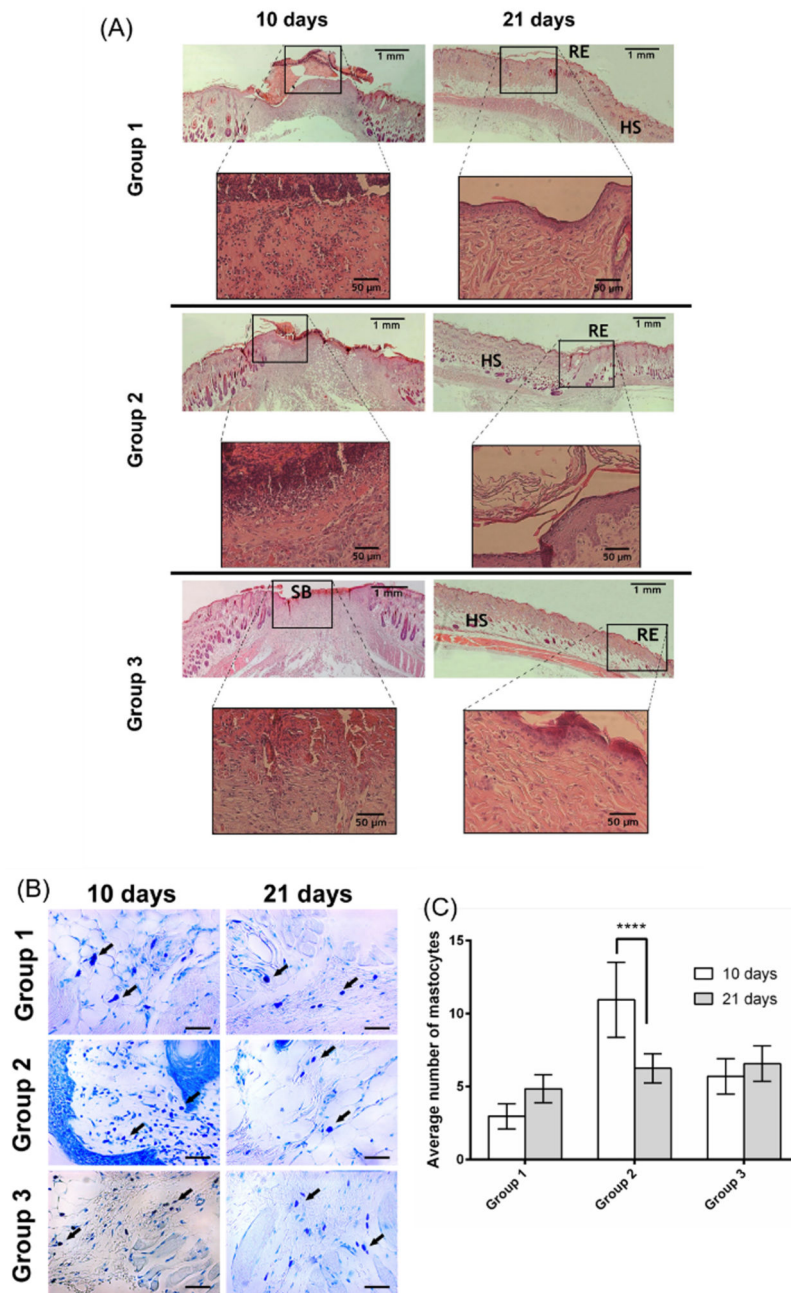


Figure 8.

Representative images of H&E-stained histological sections of explants at day 10 and 21, highlighting the wound healing progression along the time frame chosen. B) Micrographs of the different samples stained with blue toluidine after 10 and 21 days (magnification of 400x). C) Mastocyte cell number after 10 and 21 days in contact with the different materials. A p value lower than 0.001 (***) was considered statistically significant. HS: healthy skin;

RE: re-epithelization; SB:scab. Group 1 – HA membrane; Group 2 – HA-DN membrane;
Group 3 – Control.

Table 1
Histological Findings of H&E Stain

	Group 1	Group 2	Group 3
Granular Layer	+	+	-
Squamous Cell Layer	+	++	+/-
Basal Layer	+/-	+	-
Reticular Dermis	++	++	++

Note: -, low; +/-, moderate; +, much; ++, much more.